ceramics

MDPI

Article

Hydroxyapatite-Resin Composites Produced by Vat Photopolymerization and Post-Processing via In Situ Hydrolysis of Alpha Tricalcium Phosphate

Carolina Oliver-Urrutia [1], Lenka Drotárová [1], Sebastián Gascón-Pérez [1,†], Karel Slámečka [1,2], Simona Ravaszová [3], Ladislav Čelko [1] and Edgar B. Montufar [1,*]

[1] Central European Institute of Technology, Brno University of Technology, Purkyňova 123, 61200 Brno, Czech Republic; urrutia@vutbr.cz (C.O.-U.); lenka.drotarova@vut.cz (L.D.); sebastian.gascon8787@alumnos.udg.mx (S.G.-P.); slamecka@fme.vutbr.cz (K.S.); ladislav.celko@ceitec.vutbr.cz (L.Č.)
[2] Faculty of Mechanical Engineering, Brno University of Technology, Technická 2, 61669 Brno, Czech Republic
[3] Faculty of Civil Engineering, Brno University of Technology, Veveří 95, 60200 Brno, Czech Republic; ravaszova.s@fce.vutbr.cz
* Correspondence: eb.montufar@ceitec.vutbr.cz
† Current address: Centro Universitario de Ciencias Exactas e Ingenierías (CUCEI), Universidad de Guadalajara, Boulevard Marcelino García Barragán 1421, Olímpica, Guadalajara 44430, Mexico.

Abstract: Vat photopolymerization is an additive manufacturing technique that utilizes photosensitive resins to fabricate 3D polymeric objects with high precision. However, these objects often lack mechanical strength. This study investigated the strengthening of a resin based on epoxidized soybean oil acrylate, specifically designed for vat photopolymerization, by the in situ formation of hydroxyapatite nanocrystals. First, a stable alpha tricalcium phosphate (α-TCP)-resin feedstock mixture was developed (~30 vol.% α-TCP), which proved suitable for fabricating monoliths as well as complex triply periodic minimal surface (gyroid, diamond, and Schwarz) porous structures through vat photopolymerization. The results demonstrated that the incorporation of α-TCP particles led to a significant mechanical improvement of the resin. Second, post-printing hydrothermal treatments were utilized to transform the α-TCP particles into hydroxyapatite crystals within the resin. It was observed that the space between hydroxyapatite crystals within the composites was occupied by the cured resin, resulting in a more compact, stronger, and mechanically more reliable material than the porous hydroxyapatite produced by the hydrolysis of α-TCP mixed with water. Moreover, water absorption during the hydrothermal treatments caused the plasticization of the cured resin. As a consequence, the hydroxyapatite-resin composites displayed slightly lower mechanical properties compared to the as-printed α-TCP-resin composite.

Keywords: vat polymerization; alpha tricalcium phosphate; hydroxyapatite; porous composite; mechanical strength

Citation: Oliver-Urrutia, C.; Drotárová, L.; Gascón-Pérez, S.; Slámečka, K.; Ravaszová, S.; Čelko, L.; Montufar, E.B. Hydroxyapatite-Resin Composites Produced by Vat Photopolymerization and Post-Processing via In Situ Hydrolysis of Alpha Tricalcium Phosphate. *Ceramics* **2023**, *6*, 2282–2294. https://doi.org/10.3390/ceramics6040139

Academic Editor: Tatiana Safronova

Received: 26 September 2023
Revised: 17 November 2023
Accepted: 20 November 2023
Published: 24 November 2023

1. Introduction

Vat photopolymerization (VPP) is a group of additive manufacturing (AM) technologies that uses light to selectively cure a layer of a photosensitive liquid resin, producing layer-by-layer three-dimensional (3D) objects. The high precision of advanced light sources guarantees high lateral resolution during the curing process, resulting in high-quality printouts and allowing non-irradiated areas to remain liquid [1]. VPP-AM technologies are classified according to the configuration of the light source into stereolithography (SLA), digital light processing (DLP), liquid crystal display (LCD), continuous liquid interface production, two-photon polymerization, and computed axial lithography. Among them, SLA was the first and mostly used AM technology that utilizes an ultraviolet (UV) laser to cure the resin, following a scanning path for each layer of the object. On the contrary, DLP

and LCD cure a complete layer of the object in a single step by projecting the entire image of the layer in the resin, thus reducing printing time. DLP uses a digital light projector to generate the image of the layer, whereas LCD produces the image by selectively blocking a backlight, allowing the light to pass only through the areas that form the layer. LCD printers are more cost-effective and consume less power than DLP printers, making them the most common commercially available option. In addition, VPP technologies are categorized as top-down or bottom-up setups. The bottom-up approach is more common, with the light source positioned below a transparent window at the bottom of the vat, while the building platform moves upwards to create each new layer. The narrow gap between the bottom of the vat and the building platform enables better *Z* resolution than the top-down setup, but requires low viscosity resins to quickly fill the gap [2]. Moreover, each cured layer adheres to the bottom of the vat, requiring the careful lifting of the platform to detach it before building the next layer. The coating of the vat with a hydrophobic layer reduces the adhesive force preventing delamination or detachment of the object from the building platform.

The composition of the photosensitive resin is a balanced mixture of oligomers, monomers, photo initiator, and other additives [3], ensuring a fast-curing process at a specific wavelength (typically between 355 and 410 nm) with minimal photopolymerization shrinkage. Commercially available resins are generally safe, offer stable printing performance, and are available in various colors, making them ideal for producing models and prototypes. However, standard resins used in VPP printing result in printouts with poor mechanical properties that are unsuitable for structural applications. Consequently, efforts have been made to improve mechanical behavior by reinforcing the cured resins with additional phases, leading to the development of polymeric matrix composites [2,4–6]. Nanofillers play a crucial role in reinforcing the matrix due to their high specific surface area, which creates a strong interphase with the matrix [6]. This interphase increases the mechanical strength through interfacial stress transfer, crack bridging, and crack deflection. The homogeneous dispersion of the nanofiller is a microstructural requirement for these mechanisms to act efficiently. Agglomerations of the nanofillers generate stress concentration regions that decrease the fracture resistance. However, maintaining dispersion during mixing and photopolymerization is challenging due to the tendency of the nanofillers to reduce their high surface energy and increase the entropy of the system by self-aggregation. Additionally, fillers can absorb and scatter light [3] and significantly increase the viscosity of the resin [2], compromising the VPP process. Consequently, there is a limit to the amount of reinforcement that can be incorporated into the resin. Therefore, an intriguing approach is the in situ formation of nanofillers within the resin. For example, a sol–gel process in acidic vapors and the thermal reduction of metallic salts were used to induce the condensation of silica [7], and silver [8] nanoparticles, respectively, inside VPP structures. These approaches have demonstrated the potential to double the mechanical strength; however, the achieved values remained below a couple of megapascals [7].

This work explores a different approach to reinforce a commercial VPP resin through incorporating hydroxyapatite nanocrystals produced in situ by the hydrolysis of alpha tricalcium phosphate (α-TCP). α-TCP is frequently used in calcium phosphate cements (CPCs) due to its dissolution–precipitation reaction when exposed to water, resulting in the formation of a mechanically entangled network of calcium-deficient hydroxyapatite (CDHA) nanocrystals (Equation (1)) [9,10]. This reaction effectively transforms the α-TCP paste into a solid CDHA monolith, with the mechanical strength increasing as the conversion proceeds and the crystal network develops [10].

$$3\alpha\text{-}Ca_3(PO_4)_2 + H_2O \rightarrow Ca_9(HPO_4)(PO_4)_5(OH) \quad (1)$$

In previous works, non-reactive calcium phosphate powders have been incorporated into photosensitive resins to produce dense ceramic structures aided by VPP [11–17]. The goal of these studies was to achieve a maximum solid loading in the slurries without causing a detrimental increase in viscosity that could impair the layer-by-layer photopolymerization process. The resin is removed after fabrication by heating the composite in air, and then the

resulting green body is sintered at a high temperature to produce dense or porous ceramic monoliths. In contrast, the present method enables the fabrication of reinforced composites at low temperature, without the need for additional heat.

The novelty of this work was to explore if α-TCP powder incorporated in the resin reacts as a traditional CPC and to determine if the post-printing hydrolysis increases the mechanical strength of the cured composite. Initially, an α-TCP-based resin suitable for LCD VPP was developed, followed by an examination of the chemical, microstructural, and mechanical changes during hydroxyapatite formation. Subsequently, three distinct triply periodic minimal surface (TPMS) porous composite structures (i.e., gyroid, diamond, and Schwarz) were produced to compare their compression behavior.

2. Materials and Methods

2.1. Feedstock Materials

The photopolymerizable ceramic-resin slurry used in all the experiments was based on α-TCP powder and a commercial low-viscosity resin that polymerizes at 405 nm (white plant-based UV resin, Anycubic Co., Shenzhen, China). The exact formulation of the resin is not available but it is based on epoxidized soybean oil acrylate monomer, which polymerizes through the free acrylate radicals. The α-TCP was synthesized by a solid-state reaction between $CaCO_3$ and $CaHPO_4$ in a molar ratio of 1:2. The synthesis was performed at 1400 °C for 2 h with a heating rate of 2.5 °C/min, followed by air quenching. The resulting α-TCP block (150 g) was then dry milled in a planetary mill (Fritsch Pulverisette 6, Idar-Oberstein, Germany) for 15 min at 450 rpm. An agate jar (500 mL) and 25 agate balls (diameter of 20 mm) were used during the milling process. The powder fraction below 32 μm was obtained by sieving, and it was mixed with the resin at a liquid to powder (L/P) ratio of 0.70 mL/g (32 vol.%). This mixture was used as feedstock in all the experiments.

2.2. Vat Photopolymerization

The ceramic structures were produced using a bottom-up LCD printing machine (Photon Mono X, Anycubic Co., Shenzhen, China) with a pixel resolution of 50 μm at a wavelength of 405 nm. The 3D models of the structures were created in a computer design software and were saved as stereolithography (STL) files. These STL files were then exported into the printer software. The fabrication parameters were set as follows: a layer thickness of 75 μm, a normal exposure time of 10 s, an off time of 0.5 s, a bottom exposure time of 100 s, and a number of bottom layers of 6. After the printing process, any excess of unreacted feedstock resin in the printouts was removed with ethanol, and an additional curing step at 405 nm was conducted for 2 min. The composite structures, after polymerization and prior to any treatment, were labelled as α-TCP/R.

2.3. Hydrothermal Treatments

The investigation of chemical, microstructural, and mechanical changes during CDHA formation was performed using cylindrical α-TCP/R monoliths with a diameter of 6 mm and a height of 12 mm. These cured monoliths were immersed in water at different temperatures and for different durations to obtain CDHA-resin composites. The immersion conditions included 37 °C for 10 days (CDHA/R-37), 90 °C for 1 day (CDHA/R-90), and 190 °C for 30 min in an autoclave (CDHA/R-190). Monoliths consisting solely of resin (Resin), and monoliths composed of α-TCP powder mixed with 2.5% Na_2HPO_4 solution (L/P = 0.70 mL/g) hardened in water at 37 °C for 10 days (CDHA-ctrl), were used as references. The addition of Na_2HPO_4 solution aimed to enhance the cohesion of the α-TCP powder before immersion in water.

2.4. Fabrication of Porous Structures

Three different types of TPMS porous structures were fabricated with a porosity of 50%. These structures were based on isotropic gyroid, diamond, and Schwarz unit cells, respectively. The porous structures were cylinders (20 mm diameter, 10 mm height)

designed in silico with 6-unit cells along the diameter. After fabrication, the porous structures were hydrothermally treated at 90 °C for 1 day.

2.5. Physicochemical and Structural Characterization

Crystalline phases were identified by X-ray diffraction (XRD, SmartLab 3 kW CF2, Rigaku, Japan). Measurements were carried out in Bragg–Brentano parafocusing geometry at 40 kV and 30 mA, producing CuK_α radiation with λ = 0.154 nm. The scanning 2θ range was set between 10 and 90°, with a step of 0.02° and a scanning speed of 4°/min. Phase identification was performed with PDXL software (Rigaku, Japan), using structural models for α-TCP (Inorganic Centre for Diffraction Data (ICDD) No. 01-070-0364), beta tricalcium phosphate (β-TCP, ICDD No. 01-070-2065), and hydroxyapatite (ICDD No. 01-073-1731). Crystallite size was evaluated from the XRD data (hydroxyapatite peak (002) at around 25.8°) using the Debye–Scherrer approximation with a broadening constant of 0.9 [18]. Chemical changes were investigated by attenuated total reflectance Fourier transform infrared spectroscopy (ATR-FTIR, Vacuum FTIR Vertex 70v, Bruker, Bremen, Germany). Scans were performed in the MIR spectral range between 400 and 4000 cm^{-1}, averaging 40 scans with a spectral resolution of about 2 cm^{-1}. ATR-FTIR spectra were analyzed in the OPUS software (Bruker, Bremen, Germany). Powder samples for XRD and FTIR analysis were prepared by grinding two cylinders per series with sandpaper.

The microstructure was examined using scanning electron microscopy (SEM, Lyra3, TESCAN, Brno, Czech Republic) operated at an acceleration voltage of 5 kV. Before imaging, the surfaces were coated with a nanometric carbon layer. The mechanical strength and Young's modulus in compression were determined using a universal testing machine (Instron 8874, Norwood, MA, USA). The tests (n = 5) were conducted at a constant crosshead speed of 1 mm/min. The stress–strain curves were obtained from the recorded force-displacement data, with load chain compliance compensation.

The macro porosity of the porous structures (n = 5) was estimated by gravimetric analysis according to the Equation (2).

$$P = \left(1 - \frac{D_1}{D_2}\right)100, \quad (2)$$

where D_1 is the apparent density of the porous structures, calculated by dividing the mass by the bulk volume, and D_2 is the experimental density of the CDHA/R-90 dense composite (1.7 g/mL). The height and diameter of the samples were measured with a calliper to determine the volume.

3. Results

3.1. Polymerization Process and as Printed Structures

The fabrication of CDHA-resin composites by LCD VPP was successfully accomplished (Figure 1). The composite resin based on α-TCP had low viscosity, allowing smooth flow of the resin between layers without requiring additional mechanical aid. Furthermore, the composite resin did not harden spontaneously due to the hydrolysis of α-TCP, making it possible to store the resin protected from light for at least one year without any noticeable changes in viscosity or the modification of the XRD pattern.

The α-TCP/R printouts appeared white in color as both the resin and α-TCP were originally white. The composites exhibited a ceramic-matte surface, whereas the pure resin was brighter (Figure 2a). The α-TCP remained unreacted during the photopolymerization process, as the XRD pattern of the α-TCP/R monoliths mainly showed peaks indexed as α-TCP, one additional diffraction peak associated with the cured resin, and a relatively small presence of the β-TCP phase (Figure 3). Consistently, the microstructure of the α-TCP/R composite consisted of unreacted α-TCP particles embedded in the resin matrix (Figure 2a). The Resin itself showed a smooth microstructure (Figure 2a) and XRD crystallinity with a main diffraction peak at 35.5° (Figure 3).

Figure 1. STL models and VPP CDHA/R-90 porous structures.

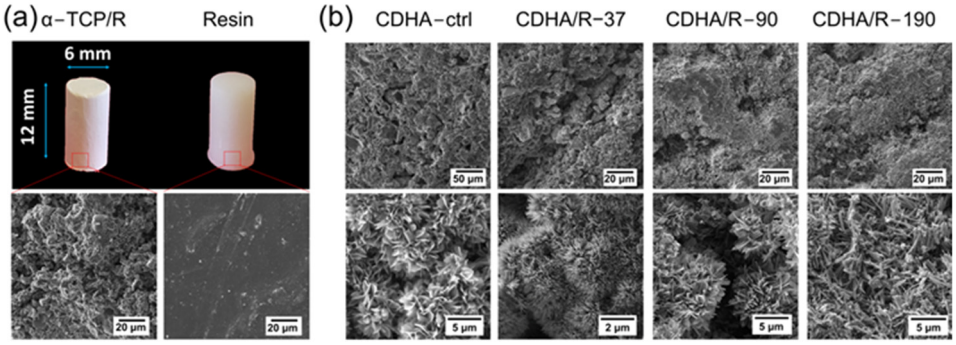

Figure 2. Microstructure of VPP composites. (**a**) α-TCP/R monolith (left) and cured resin without ceramic powder (right). (**b**) Hydrothermally treated CDHA-resin composites.

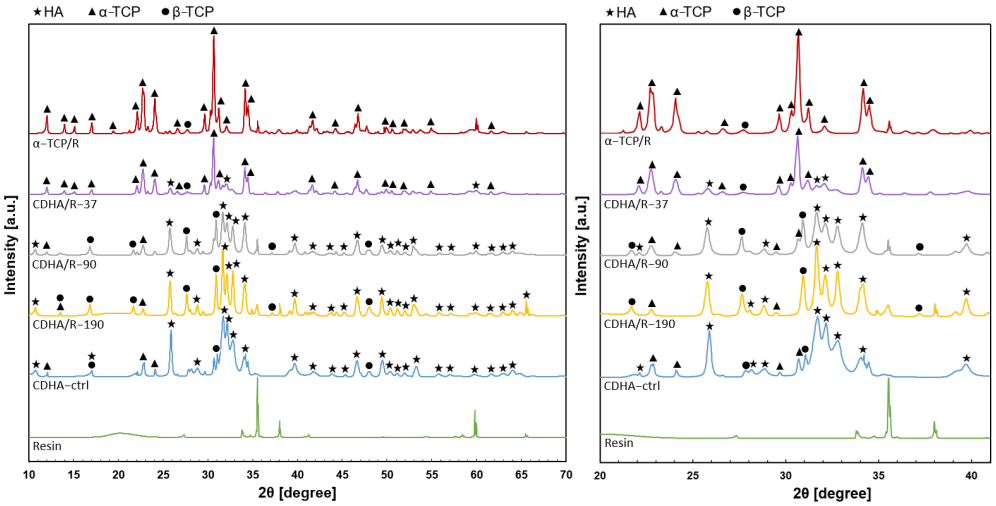

Figure 3. XRD patterns of composites fabricated by VPP. Composite components (Resin and CDHA-ctrl) are included for comparison. Right hand plot is a detailed view of the patterns in the range 20–41°.

3.2. Hydrothermal Treatment

The development of an entangled network of nanocrystals in the composites demonstrated the transformation of α-TCP into CDHA during hydrothermal treatments (Figure 2b). In general, these treatments resulted in an average diametral expansion of 3.1 ± 0.8%. The CDHA formation occurred more rapidly at a higher hydrolysis temperature as evidenced by the decrease in the intensity of the characteristic α-TCP diffraction peaks and the increasing intensity of hydroxyapatite-related peaks with increasing temperature (Figure 3). In particular, at 190 °C, the α-TCP diffraction peaks almost disappeared, although the hydrothermal treatment lasted only 30 min. The intensity of the diffraction peaks related

to β-TCP remained unchanged at 37 °C but progressively increased at a higher reaction temperature, consistent with previous works that reported the polymorphic transformation of α-TCP into β-TCP under hydrothermal conditions [19,20]. The temperature of the hydrothermal treatment also influenced the microstructure of the CDHA-resin composites. Plate-like CDHA nanocrystals were produced in the CDHA/R-90 composite and the CDHA-ctrl, whereas needle-like CDHA nanocrystals were formed in the CDHA/R-37 and CDHA/R-190 composites (Figure 2b). The crystal size was determined to be 23.5 nm for CDHA/R-37, 29.6 nm for CDHA/R-90, and 32.3 nm for CDHA/R-190, indicating faster growth of CDHA crystals at a higher hydrolysis temperature.

IR absorption spectra show the presence of characteristic bands of phosphate (PO_4^{3-}) groups in both the α-TCP/R and hydrothermally treated CDHA-resin composites (Figure 4). Intense broad bands between 900 and 1200 cm^{-1} and between 500 and 650 cm^{-1} represent the symmetric stretching vibration and the bending vibration of the PO_4^{3-} groups, respectively. Sharpening of the band around 1030 cm^{-1} and the splitting of the band between 550 and 650 cm^{-1} into two peaks confirm the transformation of α-TCP into hydroxyapatite. Furthermore, the presence of OH- groups in the hydroxyapatite crystalline structure was confirmed by the weak absorption bands between 3700 and 3900 cm^{-1} and the subtly appearing OH- band at 630 cm^{-1} as a shoulder of the PO_4^{3-} band. A flat weak absorption band at approximately 850 cm^{-1} is associated with P-OH stretch of the HPO_4^{2-} group, which is typical for calcium-deficient apatites, thus showing the formation of CDHA rather than stochiometric hydroxyapatite, which is typical for the hydroxyapatite structure formed by α-TCP hydrolysis [10].

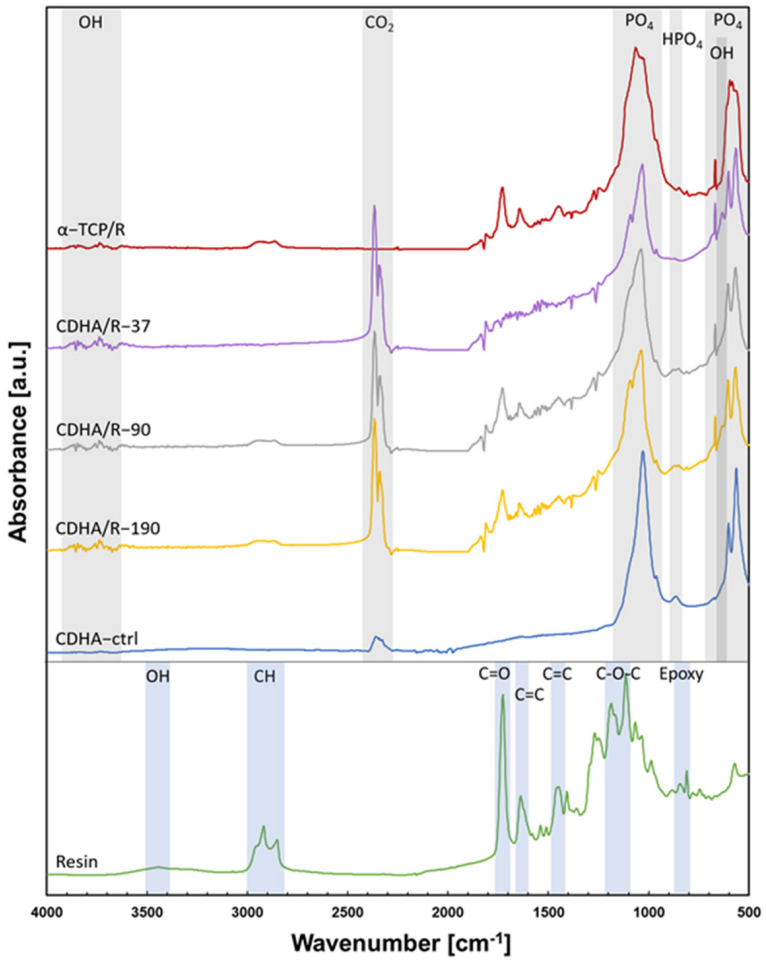

Figure 4. ATR-FTIR spectra of composites fabricated by VPP. Composite components (Resin and CDHA-ctrl) are included for comparison.

The FTIR spectrum of the cured resin demonstrates a typical high-intensity band of the carbonyl group at 1730 cm^{-1}. The bands originating from C=C stretch appear at 1630 and 1440 cm^{-1}, and the band of C–O–C stretching vibration of ester is situated between 1100–1200 cm^{-1}. Bands associated with epoxy and oxirane are present between 800 and 900 cm^{-1}. The weak band at 3400 cm^{-1} corresponds to the OH groups created from the ring opening of epoxide during acrylation. CH absorption bands are visible between 2800 and 3000 cm^{-1}. Therefore, the Resin shows the characteristic chemical bonds of epoxidized acrylate polymers, which is consistent with the photocurable monomer used. The characteristic bands of the resin are also present in the FTIR spectrum of the CDHA-resin composites and the α-TCP/R composite. Absorption bands in the range of 2300–2400 cm^{-1} are associated with the presence of atmospheric carbon dioxide absorbed on the surface of the samples.

3.3. Mechanical Characterization

The compressive stress–strain curves of the studied materials were reproducible and exhibited distinct mechanical behavior of pure components and composites (Figure 5a). The CDHA-ctrl material was weak and brittle, while the Resin demonstrated plastic behavior with a yield strength that was significantly higher than the compressive strength of the CDHA-ctrl. The plastic deformation of the Resin followed a non-linear strain hardening trend, and the tests were stopped before the Resin fracturing. Both CDHA-ctrl and the Resin had similar Young's modulus values (Figure 5c). The stress–strain curves of the composites, including the α-TCP/R, displayed three distinct domains: an initial linear elastic region, followed by nearly linear strain hardening after yielding, and finally, fast strain softening after failure at the compressive strength (Figure 5a).

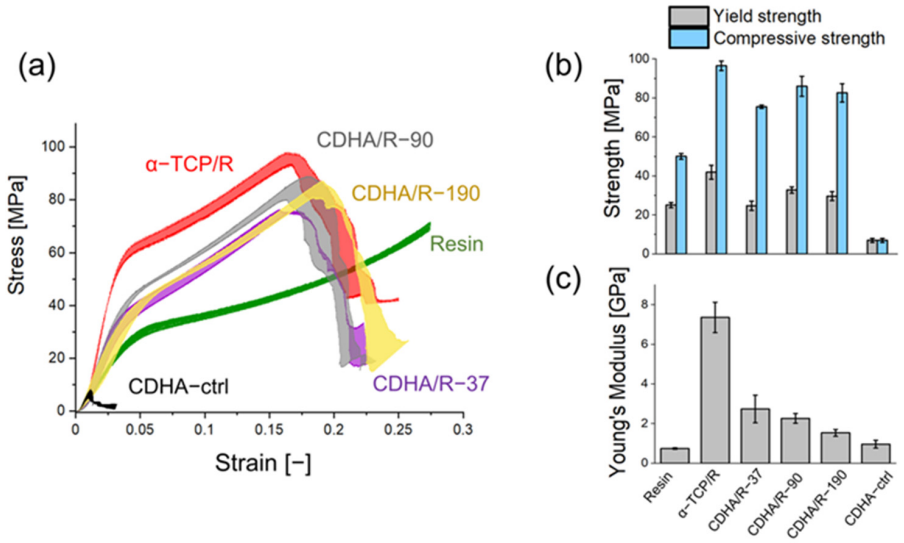

Figure 5. Results of compression tests of composite monoliths and composite components. (**a**) Compressive stress–strain curves with the highest and lowest values. (**b**) Yield strength and compressive strength. The compressive strength of the Resin corresponds to the stress at 20% strain. (**c**) Young's modulus. Bar plots show average ± SD values (n = 5).

As expected, all the composites were stronger than both the Resin and CDHA-ctrl. However, contrary to expectations, the α-TCP/R composite was the strongest one, with the yield and compressive strength that were twice as high as that of the Resin (Figure 5b), and the Young's modulus that was ten times higher (Figure 5c). Hydrothermally treated composites were found to be weaker than the α-TCP/R composite due to water absorption in the resin matrix, causing plasticization by intermolecular hydrocarbon gliding effects [21]. Nonetheless, water absorption also enabled the hydrolysis of α-TCP to form in situ reinforcing nanometric CDHA crystals (Figure 2b). The crystals counteracted matrix

softening and minimized the loss of mechanical strength. The morphology and degree of formation of CDHA produced by the different hydrothermal treatments influenced the mechanical properties. The CDHA/R-37 composite exhibited the lowest yield and compressive strength (Figure 5b) due to the incomplete transformation of α-TCP into CDHA (Figure 3). In contrast, CDHA/R-90 and CDHA/R-190, which nearly fully converted into CDHA, retained higher mechanical strength. Moreover, CDHA/R-90 was slightly stronger than CDHA/R-190 because the plate-like crystal morphology generates stronger crystal interlocking than needle-like morphology at the same porosity [22]. It is worth noting that the decline in Young's modulus followed a significantly different trend than the compressive strength. In general, the hydrothermal treatments resulted in a three-fold reduction in Young's modulus with respect to the as-printed condition (α-TCP/R). Moreover, there was a further reduction in Young's modulus with a higher temperature and shorter reaction time, indicating that temperature played a more significant role in water adsorption within the composites than time.

3.4. TPMS Porous Composite Structures

Three TPMS porous CDHA/R-90 structures were fabricated to demonstrate the suitability of the α-TCP-based resin in producing complex 3D objects (Figure 1). The porous structures exhibited high fidelity, with well-defined edges and contours (Figure 6). The surfaces of the structures were rough with a periodic pattern generated by layer-by-layer fabrication (Figure 7b,c), which is typical for VPP parts [23]. The average experimental porosity was 31.5 ± 6.1% for Schwarz, 36.7 ± 5.9% for gyroid, and 30.2 ± 3.0% for diamond structures. As expected, the porous structures exhibited lower compressive strength than the monolithic composite. In addition, the stress–strain response of the porous structures differed, showing in general a quasi-brittle behavior without a pronounced strain-hardening region (Figure 7a). This distinction is explained by local tensile stresses acting on the walls of the structures, leading to their localized failure. The presence of cup and cone fractures observed on the fracture surfaces (Figure 7b,c) further supports this hypothesis, as they are typical for polymers subjected to tension [24]. In the gyroid structures, cracks propagated at an angle of approximately 45° to the applied loading (Figure 7b), whereas in the diamond structures, cracks propagated parallel to the loading (Figure 7c). In both cases, several cracks propagated through the layers rather than between them. At a nearly constant porosity and different pore size, the Schwarz structure was stronger (34.9 MPa) than gyroid (16.3 MPa) and diamond (16.1 MPa) structures, which showed similar stress–strain responses with significant straining.

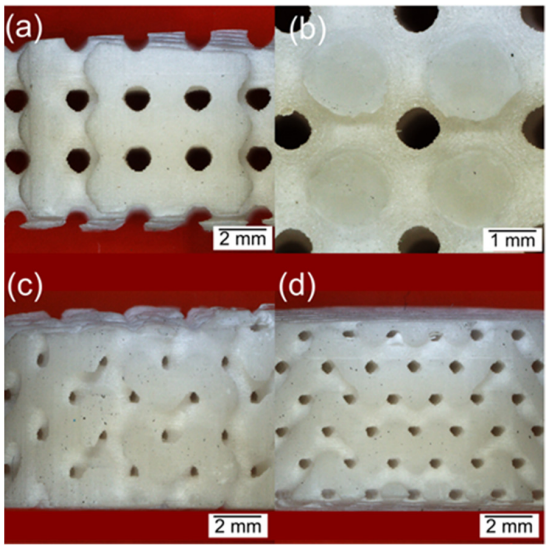

Figure 6. Images of CDHA/R-90 porous structures. (**a**) Schwarz lateral view, (**b**) Schwarz top view, (**c**) gyroid lateral view, and (**d**) diamond lateral view.

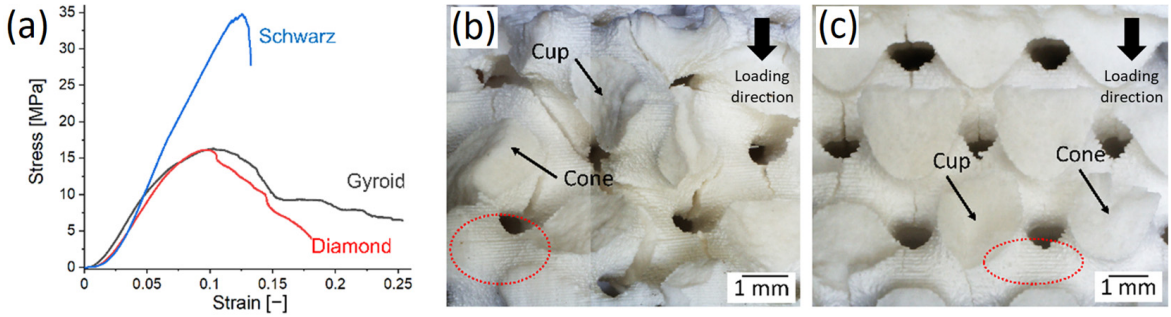

Figure 7. Mechanical behavior of CDHA/R-90 porous structures. (**a**) Compressive stress–strain curves, and images of fracture surfaces in (**b**) gyroid and (**c**) diamond TPMS porous structures. Thin arrows point to the cup and cone fractures and dash ellipses show examples of the periodic rough surface.

4. Discussion

The objective of this study was to enhance the mechanical strength of photosensitive resins to expand the potential applications of VPP parts beyond modelling and prototyping. The hydrolysis of α-TCP was explored as a straightforward method to form nanometric hydroxyapatite reinforcement crystals in a commercial photocuring resin. The resin itself did not induce the hydrolysis of α-TCP due to the absence of water molecules, ensuring the stability and printability of the feedstock mixture over an extended period. Furthermore, the α-TCP particles had a minimal impact on light absorption and scattering at the printing wavelength due to a low refractive index of 1.63 [11]. This characteristic allowed for the incorporation of a relatively high-volume fraction of reinforcement particles (32 vol.%) without hindering the selective photopolymerization of the resin and, consequently, the layer-by-layer fabrication of TPMS porous structures. The fraction of α-TCP particles incorporated in the resin (55.4 wt.%) exceeded the fraction of other fillers typically added to photopolymerizable resins (usually below 20 wt.% [25–29]), but it remained relatively low (0.7 mL/g) compared to the L/P ratio used in commercial formulations of CPCs (e.g., 0.22–0.25 mL/g [30]). The selected experimental L/P ratio allowed quick and smooth flow of the resin between layers without the need for a recoating mechanism, which is not typically included in standard VPP printers, and avoided additional steps that could increase the processing time. Based on the observations and the performance of other resins containing calcium phosphate particles [12], it is possible to increase the fraction of α-TCP up to at least 60 vol.% while maintaining a curing depth above 0.9 mm.

The incorporation of micrometric α-TCP particles alone had a significant reinforcing effect on the cured resin (Figure 5). This resulted in the Young's modulus four times higher and compressive strength in the upper range of tensile strength compared to other particle-reinforced photocurable resins [25,27,31–33]. The reinforcement effect can be attributed to the close and continuous interfacial contact between the particles and the polymeric matrix, which is promoted by strong molecular interactions, i.e., hydrogen bonds and other dipole–dipole attractions. Previous studies have explored the mixing of β-TCP particles with non-photocurable poly(methyl methacrylate) (PMMA) cements to improve the attachment with bone tissue [34–36]. However, unlike the findings of this study, the particles reduced the mechanical strength in the absence of a compatibilizer due to hydrophobic–hydrophilic immiscibility. In contrast, when the appropriate compatibilizer was utilized along with 50 wt.% of particles, the compressive strength improved to approximately 80 MPa (vs. 58 MPa in the composite without the compatibilizer) [37]. This highlights the importance of the chemical interactions at the molecular scale in influencing the mechanical behavior. However, no noticeable band shifts or interactions were observed in the FTIR analyses of the composites in this study and further research utilizing resins with lower chemical complexity is required to gain a deeper understanding of these interactions.

The results of this study demonstrate, for the first time, that the hydrolysis of α-TCP within the cured resin is possible through post-printing hydrothermal treatments. However, this achievement was not straightforward [38] because the hydrolysis reaction requires the absorption and diffusion of water through the polymeric matrix. The hydrolysis process produces in situ an entangled network of CDHA nanocrystals, which closely resembles the hardening mechanism observed in CPCs [10]. The extent of conversion into CDHA, as well as the size and morphology of the crystallites, can be controlled by adjusting the reaction temperature [22]. However, it should be noted that a higher temperature also led to the formation of a β-TCP phase at the expense of CDHA. Additionally, water absorption also solubilizes the crystalline domains in the polymeric matrix. Consequently, the CDHA-resin composites were weaker than the α-TCP/R ones. This weakening effect is particularly evident in terms of stiffness, as it is more influenced by the intermolecular hydrocarbon gliding effects than the strength.

Unlike traditional CPCs that are mixed with water-based liquids, the CDHA-resin composites exhibit a unique characteristic where the inter-crystalline space (intrinsic porosity) is filled with the cured resin. This results in a more compact material than CDHA-ctrl (traditional CPC). Consequently, the CDHA-resin composites demonstrate a remarkable strength advantage, being at least 3.7 times stronger than the CPC, and having a yield strength within the compressive strength range of stronger and less porous CPCs [22,39]. Additionally, they exhibit approximately twice the compressive strength of the Resin, approaching the mechanical strength required for structural applications. An important feature of the CDHA-resin composites is their plastic mechanical behavior, which enhances their reliability for load-bearing applications, as opposed to brittle failure. While some CPC formulations include polymers to reduce their inherent brittleness [22,40–43], these polymers are not photosensitive and cannot be processed using VPP. Therefore, this study represents the first attempt to process a CPC by VPP. Despite encountering various challenges, such as reducing the L/P ratio and preventing resin softening, this work establishes a proof of concept through the successful fabrication of three TPMS porous structures with well-defined features.

Porous materials find diverse applications in various fields, including lightweight structures, energy absorption, medical implants, heat exchangers, chemistry, fluid storage and transport, acoustic and vibrational damping, among others. TPMS porous structures, such as gyroid, diamond, and Schwarz, are particularly valuable for lightweight structural applications due to their zero-mean curvature, which eliminates stress concentrators. The mechanical properties of these structures were examined in relation to their topology by fabricating them at a constant porosity. However, the experimental porosity was generally 15 to 20% lower than the intended design porosity due to light scattering during polymerization and slight material expansion during hydrothermal treatment. Among the TPMS structures, the Schwarz structure showed the highest compressive strength because of their stretch-dominant deformation [44]. In contrast, the gyroid and diamond structures had lower strength due to their bending-dominant behavior. However, their ability to form multiple non-catastrophic cracks allowed for larger strain before failure, resulting in a higher energy absorption capacity compared to the Schwarz structure. Moreover, the diamond and gyroid structures possess more tortuous pore networks compared to the Schwarz structure, making them suitable for specific applications that require enhanced interaction of the material with a fluid.

5. Conclusions

The successful fabrication of α-TCP-resin composites using LCD VPP was achieved. Hydrothermal treatments allowed the hydrolysis of α-TCP within the resin to form nanometric CDHA crystals, resembling the hardening process of CPCs. It was observed that a higher temperature led to a faster α-TCP hydrolysis and the formation of larger CDHA crystals. The CDHA-resin composites were more compact and stronger materials compared to CDHA-ctrl and other traditional CPCs. The inter-crystalline space within the compos-

ites was filled with the cured resin, contributing to the improved mechanical reliability. Moreover, all the composites were stronger and therefore more suitable for load-bearing applications than the commercial photopolymerizable resin. Water absorption facilitated α-TCP hydrolysis but also caused plasticization of the polymeric matrix due to solvation of the crystalline domains. Consequently, the α-TCP/R composite displayed the highest mechanical properties among the different composites. The TPMS porous composite structures showed a quasi-brittle mechanical behavior. Among them, the Schwarz structure demonstrated the highest compressive strength, whereas gyroid and diamond structures had a higher energy absorption capacity at a porosity level of about 30–36%.

Author Contributions: C.O.-U.: Conceptualization, Investigation, Formal analysis, Writing—review. L.D.: Investigation, Formal analysis, Writing—review & editing. S.G.-P.: Methodology, Investigation, Writing—review and editing. K.S.: Methodology, Investigation, Writing—review and editing. S.R.: Investigation, Writing—review and editing. L.Č.: Formal analysis, Writing—review and editing, Funding acquisition, Recourses. E.B.M.: Conceptualization, Methodology, Writing—review and editing, Funding acquisition. All authors have read and agreed to the published version of the manuscript.

Funding: This research was funded by the Czech Ministry of Education, Youth and Sports (MEYS-CR, IMPROVE V: CZ.02.01.01/00/22_010/0002552), and the Brno University of Technology (CEITEC VUT/FAST-J-22-7956 and CEITEC VUT/FCH-J-23-8367). S.G.-P. acknowledges the scholarship ESACIES-2023 and the support provided by CUCEI, both from the Universidad de Guadalajara. Special acknowledgment is given to CzechNanoLab Research Infrastructure supported by MEYS-CR (LM2018110).

Data Availability Statement: The data generated in this study are contained within the article.

Conflicts of Interest: The authors declared no conflicts of interest with the present research, authorship or publication of this article.

References

1. Paral, S.K.; Lin, D.Z.; Cheng, Y.L.; Lin, S.C.; Jeng, J.Y. A Review of Critical Issues in High-Speed Vat Photopolymerization. *Polymers* **2023**, *15*, 2716. [CrossRef] [PubMed]
2. Medellin, A.; Du, W.; Miao, G.; Zou, J.; Pei, Z.; Ma, C. Vat Photopolymerization 3d Printing of Nanocomposites: A Literature Review. *J. Micro Nano-Manuf.* **2019**, *7*, 031006. [CrossRef]
3. Zakeri, S.; Vippola, M.; Levänen, E. A Comprehensive Review of the Photopolymerization of Ceramic Resins Used in Stereolithography. *Addit. Manuf.* **2020**, *35*, 101177. [CrossRef]
4. Vidakis, N.; Petousis, M.; Papadakis, V.M.; Mountakis, N. Multifunctional Medical Grade Resin with Enhanced Mechanical and Antibacterial Properties: The Effect of Copper Nano-Inclusions in Vat Polymerization (VPP) Additive Manufacturing. *J. Funct. Biomater.* **2022**, *13*, 258. [CrossRef] [PubMed]
5. Lala, S.D.; Deoghare, A.B.; Chatterjee, S. Effect of Reinforcements on Polymer Matrix Bio-Composites—An Overview. *IEEE J. Sel. Top. Quantum Electron.* **2018**, *25*, 1039–1058. [CrossRef]
6. Li, Y.; Wang, W.; Wu, F.; Kankala, R.K. Vat Polymerization-Based 3D Printing of Nanocomposites: A Mini Review. *Front. Mater.* **2023**, *9*, 1118943. [CrossRef]
7. Chiappone, A.; Fantino, E.; Roppolo, I.; Lorusso, M.; Manfredi, D.; Fino, P.; Pirri, C.F.; Calignano, F. 3D Printed PEG-Based Hybrid Nanocomposites Obtained by Sol-Gel Technique. *ACS Appl. Mater. Interfaces* **2016**, *8*, 5627–5633. [CrossRef]
8. Fantino, E.; Chiappone, A.; Calignano, F.; Fontana, M.; Pirri, F.; Roppolo, I. In Situ Thermal Generation of Silver Nanoparticles in 3D Printed Polymeric Structures. *Materials* **2016**, *9*, 589. [CrossRef]
9. Tronco, M.C.; Cassel, J.B.; dos Santos, L.A. α-TCP-Based Calcium Phosphate Cements: A Critical Review. *Acta Biomater.* **2022**, *151*, 70–87. [CrossRef]
10. Ginebra, M.P.; Fernández, E.; De Maeyer, E.A.P.; Verbeeck, R.M.H.; Boltong, M.G.; Ginebra, J.; Driessens, F.C.M.; Planell, J.A. Setting Reaction and Hardening of an Apatitic Calcium Phosphate Cement. *J. Dent. Res.* **1997**, *76*, 905–912. [CrossRef]
11. Paredes, C.; Martínez-Vázquez, F.J.; Elsayed, H.; Colombo, P.; Pajares, A.; Miranda, P. Evaluation of Direct Light Processing for the Fabrication of Bioactive Ceramic Scaffolds: Effect of Pore/Strut Size on Manufacturability and Mechanical Performance. *J. Eur. Ceram. Soc.* **2021**, *41*, 892–900. [CrossRef]
12. Scalera, F.; Esposito Corcione, C.; Montagna, F.; Sannino, A.; Maffezzoli, A. Development and Characterization of UV Curable Epoxy/Hydroxyapatite Suspensions for Stereolithography Applied to Bone Tissue Engineering. *Ceram. Int.* **2014**, *40*, 15455–15462. [CrossRef]

13. Lee, Y.H.; Lee, J.B.; Maeng, W.Y.; Koh, Y.H.; Kim, H.E. Photocurable Ceramic Slurry Using Solid Camphor as Novel Diluent for Conventional Digital Light Processing (DLP) Process. *J. Eur. Ceram. Soc.* **2019**, *39*, 4358–4365. [CrossRef]
14. Goutagny, C.; Hocquet, S.; Hautcoeur, D.; Lasgorceix, M.; Somers, N.; Leriche, A. Development of Calcium Phosphate Suspensions Suitable for the Stereolithography Process. *Open Ceram.* **2021**, *7*, 100167. [CrossRef]
15. Liu, Z.; Liang, H.; Shi, T.; Xie, D.; Chen, R.; Han, X.; Shen, L.; Wang, C.; Tian, Z. Additive Manufacturing of Hydroxyapatite Bone Scaffolds via Digital Light Processing and in Vitro Compatibility. *Ceram. Int.* **2019**, *45*, 11079–11086. [CrossRef]
16. Lasgorceix, M.; Champion, E.; Chartier, T. Shaping by Microstereolithography and Sintering of Macro-Micro-Porous Silicon Substituted Hydroxyapatite. *J. Eur. Ceram. Soc.* **2016**, *36*, 1091–1101. [CrossRef]
17. Mohammadi, M.; Coppola, B.; Montanaro, L.; Palmero, P. Digital Light Processing of High-Strength Hydroxyapatite Ceramics: Role of Particle Size and Printing Parameters on Microstructural Defects and Mechanical Properties. *J. Eur. Ceram. Soc.* **2023**, *43*, 2761–2772. [CrossRef]
18. Poralan, G.M.; Gambe, J.E.; Alcantara, E.M.; Vequizo, R.M. X-Ray Diffraction and Infrared Spectroscopy Analyses on the Crystallinity of Engineered Biological Hydroxyapatite for Medical Application. In *Proceedings of the IOP Conference Series: Materials Science and Engineering*; IOP Publishing: Bristol, UK, 2015; Volume 79.
19. Galea, L.; Alexeev, D.; Bohner, M.; Doebelin, N.; Studart, A.R.; Aneziris, C.G.; Graule, T. Textured and Hierarchically Structured Calcium Phosphate Ceramic Blocks through Hydrothermal Treatment. *Biomaterials* **2015**, *67*, 93–103. [CrossRef]
20. Raymond, S.; Maazouz, Y.; Montufar, E.B.; Perez, R.A.; González, B.; Konka, J.; Kaiser, J.; Ginebra, M.P. Accelerated Hardening of Nanotextured 3D-Plotted Self-Setting Calcium Phosphate Inks. *Acta Biomater.* **2018**, *75*, 451–462. [CrossRef]
21. Wang, B.; Li, D.; Xian, G.; Li, C. Effect of Immersion in Water or Alkali Solution on the Structures and Properties of Epoxy Resin. *Polymers* **2021**, *13*, 1902. [CrossRef]
22. Kashimbetova, A.; Slámečka, K.; Casas-Luna, M.; Oliver-Urrutia, C.; Ravaszová, S.; Dvořák, K.; Čelko, L.; Montufar, E.B. Implications of Unconventional Setting Conditions on the Mechanical Strength of Synthetic Bone Grafts Produced with Self-Hardening Calcium Phosphate Pastes. *Ceram. Int.* **2022**, *48*, 6225–6235. [CrossRef]
23. Golhin, A.P.; Tonello, R.; Frisvad, J.R.; Grammatikos, S.; Strandlie, A. Surface Roughness of As-Printed Polymers: A Comprehensive Review. *Int. J. Adv. Manuf. Technol.* **2023**, *127*, 987–1043. [CrossRef]
24. Rodriguez, E.L. Cup-and-Cone Fracture Surfaces in Polyvinyl Chloride Due to Tensile Fatigue. *J. Mater. Sci. Lett.* **1995**, *14*, 1230–1233. [CrossRef]
25. Weng, Z.; Zhou, Y.; Lin, W.; Senthil, T.; Wu, L. Structure-Property Relationship of Nano Enhanced Stereolithography Resin for Desktop SLA 3D Printer. *Compos. Part A Appl. Sci. Manuf.* **2016**, *88*, 234–242. [CrossRef]
26. Corcione, C.E.; Cataldi, A.; Frigione, M. Measurements of Size Distribution Nanoparticles in Ultraviolet-Curable Methacrylate-Based Boehmite Nanocomposites. *J. Appl. Polym. Sci.* **2013**, *128*, 4102–4109. [CrossRef]
27. Kumar, S.; Hofmann, M.; Steinmann, B.; Foster, E.J.; Weder, C. Reinforcement of Stereolithographic Resins for Rapid Prototyping with Cellulose Nanocrystals. *ACS Appl. Mater. Interfaces* **2012**, *4*, 5399–5407. [CrossRef]
28. Chong, Y.T.; Tan, C.S.H.; Liu, L.Y.; Liu, J.; Teng, C.P.; Wang, F.K. Enhanced Dispersion of Hydroxyapatite Whisker in Orthopedics 3D Printing Resin with Improved Mechanical Performance. *J. Appl. Polym. Sci.* **2021**, *138*, 50811. [CrossRef]
29. Makvandi, P.; Esposito Corcione, C.; Paladini, F.; Gallo, A.L.; Montagna, F.; Jamaledin, R.; Pollini, M.; Maffezzoli, A. Antimicrobial Modified Hydroxyapatite Composite Dental Bite by Stereolithography. *Polym. Adv. Technol.* **2018**, *29*, 364–371. [CrossRef]
30. Friedman, C.D.; Costantino, P.D.; Takagi, S.; Chow, L.C. Bonesource(TM) Hydroxyapatite Cement: A Novel Biomaterial for Craniofacial Skeletal Tissue Engineering and Reconstruction. *J. Biomed. Mater. Res.* **1998**, *43*, 428–432. [CrossRef]
31. Yunus, D.E.; Shi, W.; Sohrabi, S.; Liu, Y. Shear Induced Alignment of Short Nanofibers in 3D Printed Polymer Composites. *Nanotechnology* **2016**, *27*, 495302. [CrossRef]
32. Manapat, J.Z.; Mangadlao, J.D.; Tiu, B.D.B.; Tritchler, G.C.; Advincula, R.C. High-Strength Stereolithographic 3D Printed Nanocomposites: Graphene Oxide Metastability. *ACS Appl. Mater. Interfaces* **2017**, *9*, 10085–10093. [CrossRef]
33. Gonzalez, G.; Chiappone, A.; Roppolo, I.; Fantino, E.; Bertana, V.; Perrucci, F.; Scaltrito, L.; Pirri, F.; Sangermano, M. Development of 3D Printable Formulations Containing CNT with Enhanced Electrical Properties. *Polymer* **2017**, *109*, 246–253. [CrossRef]
34. Dall'Oca, C.; Maluta, T.; Cavani, F.; Morbioli, G.P.; Bernardi, P.; Sbarbati, A.; Degl'Innocenti, D.; Magnan, B. The Biocompatibility of Porous vs Non-Porous Bone Cements: A New Methodological Approach. *Eur. J. Histochem.* **2014**, *58*, 2255. [CrossRef]
35. Yang, J.; Zhang, K.; Zhang, S.; Fan, J.; Guo, X.; Dong, W.; Wang, S.; Chen, Y.; Yu, B. Preparation of Calcium Phosphate Cement and Polymethyl Methacrylate for Biological Composite Bone Cements. *Med. Sci. Monit.* **2015**, *21*, 1162. [CrossRef] [PubMed]
36. Beruto, D.T.; Mezzasalma, S.A.; Capurro, M.; Botter, R.; Cirillo, P. Use of α-Tricalcium Phosphate (TCP) as Powders and as an Aqueous Dispersion to Modify Processing, Microstructure, and Mechanical Properties of Polymethylmethacrylate (PMMA) Bone Cements and to Produce Bone-Substitute Compounds. *J. Biomed. Mater. Res.* **2000**, *49*, 498–505. [CrossRef]
37. Gao, S.; Lv, Y.; Yuan, L.; Ren, H.; Wu, T.; Liu, B.; Zhang, Y.; Zhou, R.; Li, A.; Zhou, F. Improved Bone Ingrowth of Tricalcium Phosphate Filled Poly(Methyl Methacrylate) (PMMA) Bone Cements In Vivo. *Polym. Test.* **2019**, *76*, 513–521. [CrossRef]
38. Sugawara, A.; Antonucci, J.M.; Takagi, S.; Chow, L.C.; Ohashi, M. Formation of Hydroxyapatite in Hydrogels from Tetracalcium Phosphate/Dicalcium Phosphate Mixtures. *J. Nihon Univ. Sch. Dent.* **1989**, *31*, 372–381. [CrossRef] [PubMed]
39. Gbureck, U.; Spatz, K.; Thull, R.; Barralet, J.E. Rheological Enhancement of Mechanically Activated α-Tricalcium Phosphate Cements. *J. Biomed. Mater. Res.—Part B Appl. Biomater.* **2005**, *73*, 1–6. [CrossRef] [PubMed]

40. Mickiewicz, R.A.; Mayes, A.M.; Knaack, D. Polymer-Calcium Phosphate Cement Composites for Bone Substitutes. *J. Biomed. Mater. Res.* **2002**, *61*, 581–592. [CrossRef]
41. Xu, H.H.K.; Burguera, E.F.; Carey, L.E. Strong, Macroporous, and in Situ-Setting Calcium Phosphate Cement-Layered Structures. *Biomaterials* **2007**, *28*, 3786–3796. [CrossRef]
42. Chen, W.C.; Ju, C.P.; Wang, J.C.; Hung, C.C.; Chern Lin, J.H. Brittle and Ductile Adjustable Cement Derived from Calcium Phosphate Cement/Polyacrylic Acid Composites. *Dent. Mater.* **2008**, *24*, 1616–1622. [CrossRef] [PubMed]
43. Matsuya, Y.; Antonucci, J.M.; Matsuya, S.; Takagi, S.; Chow, L.C. Polymeric Calcium Phosphate Cements Derived from Poly(Methyl Vinyl Ether-Maleic Acid). *Dent. Mater.* **1996**, *12*, 2–7. [CrossRef] [PubMed]
44. Keshavarzan, M.; Kadkhodaei, M.; Badrossamay, M.; Karamooz Ravari, M.R. Investigation on the Failure Mechanism of Triply Periodic Minimal Surface Cellular Structures Fabricated by Vat Photopolymerization Additive Manufacturing under Compressive Loadings. *Mech. Mater.* **2020**, *140*, 103150. [CrossRef]